MECSOL 2022 - Proceedings of the 8th International Symposium on Solid Mechanics
M.L. Bittencourt, J. Labaki, L.C.M. Vieira Jr. and E. Mesquita (Editors), Campinas SP, Brazil, October 17th to 19th, 2022

A time-domain IBEM-FEM model of the ground vibration attenuation function of surface walls

Leonardo Antoniazzi Marques and Josué Labaki

School of Mechanical Engineering, University of Campinas, Campinas SP Brazil

Abstract. This article presents a study on the ground vibration attenuation performance of surface walls. The analyses consider ground vibration resulting from transient impulse sources applied at the soil surface. A coupled IBEM-FEM model is used for the study, in which surface walls are modeled via classical finite elements, and the response of the soil is modeled via superposition of soil influence functions, within an Indirect Boundary Element Method (IBEM) framework. Coupling between the two subsystems is obtained by imposing continuity and equilibrium conditions at the soil–wall interface. The dynamic response of the coupled system is derived in the frequency domain, in which the coupled equations of motion can be solved algebraically. Transient responses to impulse loading are obtained from these by direct application of Fast Fourier Transforms (FFT), which require accurate evaluation of the harmonic solutions for atypically high frequencies. Selected numerical results are presented, which are focused on showing the extent to which surface walls are able to attenuate seismic excitation. The results show that surface walls can be an effective measure against ground vibration, and that their height and the material with which they are built can be selected to yield optimal attenuation performance.
Keywords: soil-structure interaction, vibration attenuation, coupled methods, transient problems, gabion walls

INTRODUCTION

Large-scale, vibration-sensitive structures like particle accelerators and nuclear powerplants have remarkably strict limits on how much their foundations are allowed to vibrate. This is due to the direct impact that ground vibration has on the proper operation and safety of installations like those. Ground vibration can originate from sources as ordinary as road and railway traffic, but also from less ordinary sources such as earthquakes, and the relevant spectrum range for large-scale structures typically falls under 100 Hz.

Various engineering solutions against ground vibration have been studied throughout the years. Casablanca et al. (2018) is one example of approach, which is based on designing sophisticated foundations that can counteract ground vibration. Kaewunruen et al. (2017) is one example of approach that proposes instead to attenuate vibrations directly at the source. The third class of approaches relies on interposing some vibration-attenuation or vibration-blocking device between the vibration source and the target structure. These include open and filled trenches (Herbut, 2020; Bose et al., 2018), elastic bodies such as piles and plates (Álamo et al., 2019; Albino et al., 2019), locally-resonant artificial or natural bodies (Colombi et al., 2016), and surface structures (Krylov, 2007), which are the object of the present paper.

This work is inspired by the proposition by Krylov (2007) that decorative roadside boulders have a role in the attenuation of the levels of vibration that propagate from the road to its surroundings. He showed that the mechanism by which boulders affect ground vibration is the scattering of Rayleigh waves into body waves, which are then partially projected into the bulk of the soil, reducing the amount of energy that is left to propagate in the original direction of propagation. Mhanna et al. (2014) and Masoumi et al. (2014) provided supporting experimental evidence that this is the case, using water tanks and concrete blocks, respectively. These results investigated separately the effect of mass and stiffness of the surface structure into the attenuation effectiveness of the surface structure. Dijckmans et al. (2015) used a combination of a simplified numerical model and extensive numerical results, and argued that the attenuation performance of gabion and concrete walls are independently related to their horizontal, rocking, and flexural modes. More recently, Carneiro et al. (2022) put forward a coupled model involving the Indirect Boundary Element Method (IBEM) to represent the soil and the classical Finite Element Method (FEM) to represent the surface structure. With this IBEM-FEM coupling model, they were able to look more closely into the mechanism of conversion from surface to body waves by surface walls. They showed that wider walls do not necessarily provide better attenuation performance, and that the anisotropy of the soil is irrelevant to the attenuation performance of the wall. The models by Dijckmans et al. (2015) and Carneiro et al. (2022) are limited in that they are only capable of representing time-harmonic phenomena. While this is sufficient to allow investigations on the relations between attenuation performance and vibration modes of walls, they are unable to represent

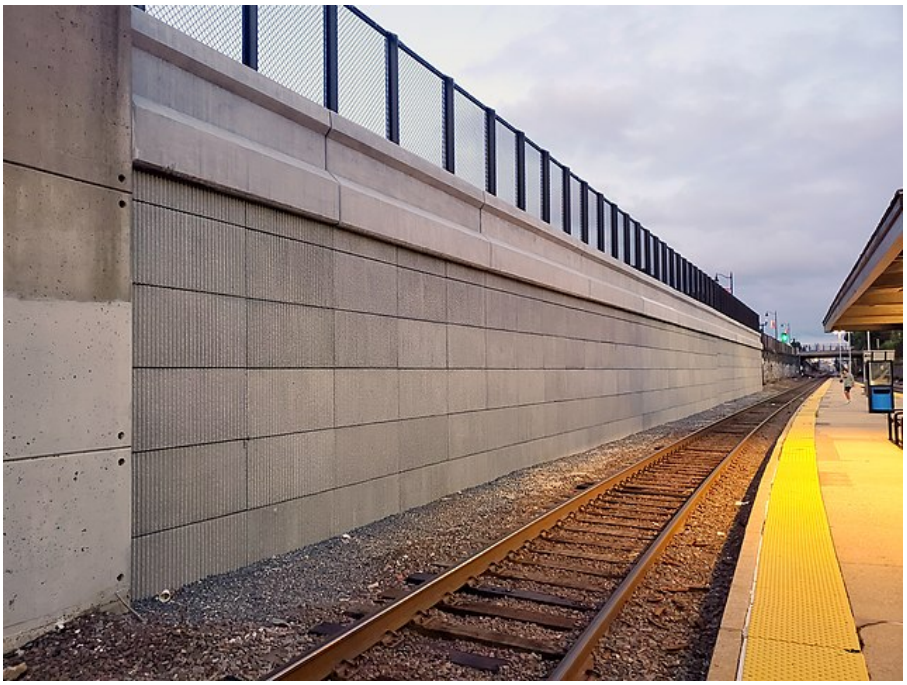

Figure 1 – The newly completed retaining wall at Porter station in Cambridge MA, USA (July 2021) may help attenuate vibration that propagates from the train track to its surroundings (author: Pi.1415926535).

transient phenomena such as earthquakes, pile drivers, and passing trains, which are common in engineering practice.

This work presents a model of the transient response of surface walls interacting with the soil. The model consists of the superposition of non-singular influence functions to represent the response of the soil, in the sense of an IBEM framework, together with the classical FEM to represent the response of the wall. Coupling between the two models is achieved in the frequency domain by imposing continuity and equilibrium conditions at the wall–soil interface. This condition results in an algebraic system of equations in the frequency domain, which can be solved for arbitrary frequencies of excitation. The transient response of the wall–soil system is obtained by subjecting its harmonic response to a Fast Fourier Transform (FFT), which results in the response of the system to an impulse load. The paper shows selected numerical results on the attenuation performance of walls with various geometric and constitutive parameters, and considers representative cases of transient excitation.

PROBLEM DEFINITION

Consider a linear-elastic prismatic wall resting in perfectly bonded contact to the surface of a linear-elastic, homogeneous, isotropic half-plane representing the soil (Fig. 2). The wall has height H, width L, and infinite length, Young's modulus E_w, Poisson ratio ν_w, and mass density ρ_w. The soil has Young's modulus E, Poisson ratio ν, and mass density ρ. In view of the infinite length that is assumed for the wall, the problem is modeled as a two-dimensional plane-strain problem, in terms of the rectangular coordinate system (x,z). The coordinate system is placed so that the center of the wall-soil interface rests at the origin. Arbitrary transient loads are uniformly distributed on a patch of width a of the surface of the soil, the center of which is at a distance d from the center of the wall. Loads can be applied in the horizontal (x) or vertical (z) directions. The problem consists in determining the response of the wall and of its surrounding soil due to these external loads. In particular, the analyses are geared towards understanding the effect of the inclusion of the wall on the levels of ground motion at the installation point ($x = z = 0$) and on its vicinity.

SOIL MODEL

Consider a two-dimensional, transversely isotropic, homogeneous half-plane, defined by four independent constitutive properties c_{11}, c_{13}, c_{33}, and c_{44} and mass density ρ, subjected to time-harmonic excitation of circular frequency ω.

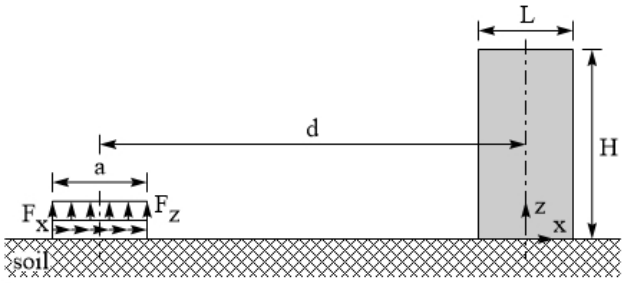

Figure 2 – Infinitely long wall on the surface of the soil, under horizontal and vertical transient loads.

Rajapakse and Wang (1991) derived solutions for the horizontal and vertical displacement fields in this medium as

$$u_{xx} = -\frac{2}{\pi c_{44}\delta}\int_0^\infty \frac{1}{R}\left(\eta_3\bar{\omega}_1 e^{\delta\xi_1 z} - \eta_4\bar{\omega}_2 e^{\delta\xi_2 z}\right)\cos(\delta\zeta x)\,d\zeta, \tag{1}$$

$$u_{zx} = -\frac{2\mathrm{i}}{\pi c_{44}\delta}\int_0^\infty \frac{1}{R}\left(\eta_3\bar{\omega}_1 e^{\delta\xi_1 z} - \eta_4\bar{\omega}_2 e^{\delta\xi_2 z}\right)\sin(\delta\zeta x)\,d\zeta, \tag{2}$$

$$u_{xz} = \frac{2\mathrm{i}}{\pi c_{44}\delta}\int_0^\infty \frac{1}{R}\left(\eta_2\bar{\omega}_1 e^{\delta\xi_1 z} - \eta_1\bar{\omega}_2 e^{\delta\xi_2 z}\right)\sin(\delta\zeta x)\,d\zeta, \tag{3}$$

$$u_{zz} = \frac{2}{\pi c_{44}\delta}\int_0^\infty \frac{1}{R}\left(\eta_2\bar{\omega}_1 e^{\delta\xi_1 z} - \eta_1\bar{\omega}_2 e^{\delta\xi_2 z}\right)\cos(\delta\zeta x)\,d\zeta, \tag{4}$$

in which u_{ij} denotes displacements in the $i-$direction due to loads in the $j-$direction, $\zeta = \lambda/\delta$, $\alpha = c_{33}/c_{44}$, $\beta = c_{11}/c_{44}$, $\kappa = (c_{13}+c_{44})/c_{44}$, $\delta^2 = \rho\omega^2/c_{44}$, and

$$R = \frac{\eta_1\eta_3 - \eta_2\eta_4}{\sin(\delta\zeta b)}\zeta, \tag{5}$$

$$\xi_{1,2}^2 = \left(\gamma\zeta^2 - 1 - \alpha \pm \sqrt{\Phi}\right)/(2\alpha), \tag{6}$$

$$\Phi = \left(\gamma\zeta^2 - 1 - \alpha\right)^2 - 4\alpha\left[\beta\zeta^4 - (1+\beta)\zeta^2 + 1\right], \tag{7}$$

$$\gamma = 1 + \alpha\beta - \kappa^2, \tag{8}$$

$$\bar{\omega}_i = \left(\alpha\xi_i^2 - \zeta^2 + 1\right)/(\mathrm{i}\kappa\zeta\xi_i), \tag{9}$$

$$\eta_{1,2} = -\xi_{1,2}\bar{\omega}_{1,2} + \mathrm{i}\zeta, \tag{10}$$

and

$$\eta_{3,4} = (\kappa - 1)\,\mathrm{i}\zeta\bar{\omega}_{2,1} - \alpha\xi_{2,1}. \tag{11}$$

The present case of an isotropic half-plane is a particular case of the above, where

$$c_{11} = c_{33} = \frac{E(1-\nu)}{(1+\nu)(1-2\nu)}, \tag{12}$$

$$c_{12} = c_{13} = \frac{E\nu}{(1+\nu)(1-2\nu)}, \tag{13}$$

and

$$c_{44} = G = \frac{E}{2(1+\nu)}, \tag{14}$$

in which G is the shear modulus. A detailed description of the strategy used in this paper for the numerical evaluation of Eqs. 1 to 4 is presented in Labaki et al. (2012).

WALL MODEL

Since the wall is a simple linear-elastic finite body, in this paper we use classical finite elements to model its response. In this model, four-noded quadrilateral elements are used, which have two displacement degrees of freedom per node. The equation of motion for the wall is given by

$$\bar{K}u = f, \tag{15}$$

in which $\bar{K} = K - \omega^2 M$ is the dynamic stiffness matrix of the wall, and u and f are the vectors of displacements and forces at the nodes (Bathe, 2006).

WALL–SOIL COUPLING

Equation 15 can be modified to represent the interaction between the wall and the soil. This comprises the inclusion of interface forces f_s that arise at the bottom of the wall due to the presence of the soil. This modified equation of motion for the nodes at the interface (denoted by an apostrophe) can be written as

$$\bar{K}'u' = f' - f_s. \tag{16}$$

The distribution of contact forces f_s experienced at the nodes of the wall must maintain equilibrium with the contact tractions experienced by the soil at the wall–soil interface. This distribution is unknown, and can be approximated by piece-wise constant fictitious contact tractions q, which are also unknown. The equilibrium condition between f_s and q can be stated as

$$f_s = Aq, \tag{17}$$

in which A is a purely geometric transformation matrix. In view of this transformation, Eq. 16 can be rewritten as

$$\bar{K}'u' + Aq = f'. \tag{18}$$

In addition to the equilibrium condition, a continuity condition must be imposed at the wall–soil interface. This condition can be stated as

$$w_s = Uq, \tag{19}$$

in which w_s is the vector of nodal displacements of the soil at the interface, and U is the influence matrix of the soil, the terms of which come from Eqs. 1 to 4. Displacements of the soil at the interface, w_s, can be written in terms of displacements of the wall at the interface, u' (Eq. 16) as

$$w_s = Du', \tag{20}$$

in which D is a purely geometric transformation matrix. The continuity condition then yields

$$Du' - Uq = 0. \tag{21}$$

The reader may refer to Carneiro et al. (2022) for an expression of transformation matrices A and D. The continuity condition expressed by Eq. 21 corresponds to the condition that the wall is in perfectly bonded contact with the soil, which is a reasonable hypothesis for the case of heavy walls and low frequency of excitation considered in this paper.

Equations 18 and 21 can be combined into one equation of motion for the nodes at the wall–soil interface:

$$\begin{bmatrix} \bar{K} & \begin{bmatrix} 0 \\ A \end{bmatrix} \\ \begin{bmatrix} 0 & D \end{bmatrix} & -U \end{bmatrix} \begin{Bmatrix} u \\ q \end{Bmatrix} = \begin{Bmatrix} f \\ 0 \end{Bmatrix}. \tag{22}$$

This equation of motion must be incorporated into the equation of motion for the whole wall. Solving the new equation of motion for a set of external loads f results in the nodal displacements u of the nodes of the wall, and in the fictitious contact tractions q at the interface, from which solutions anywhere in the soil can be computed (Carneiro et al., 2019).

TRANSIENT SOLUTIONS

In this paper, transient solutions are obtained by applying a space transform to a vector of discrete time-harmonic solutions resulting from the solution of Eq. 22. The space transform used is the Fourier transform and its inverse, the discrete form of which is expressed by

$$\mathcal{F}(x_n) = X_k = \sum_{n=0}^{N-1} x_n \mathrm{e}^{-\mathrm{i}2\pi kn/N} \tag{23}$$

and

$$\mathcal{F}^{-1}(X_k) = x_n = \frac{1}{N}\sum_{k=0}^{N-1} X_k \mathrm{e}^{\mathrm{i}2\pi kn/N}, \tag{24}$$

in which x_n and X_k are discrete vectors of size N of the signal in the frequency and time domains, respectively. In this analysis, we use the Fast Fourier Transform (FFT), a computationally efficient algorithm to evaluate Eqs. 23 and 24 implemented in Matlab. Although the FFT is a widely used tool to obtain transient solutions from harmonic ones and vice-versa, it is not commonly applied to soil problems due to the difficulty in obtaining solutions for these media at high frequencies. In view of their application to soil vibration problems, the frequency of interest of which are typically very low, classical implementations are normally not planned to be able to yield accurate solutions at high frequencies. However, solutions at higher frequencies are necessary to obtain accurate transient solutions through the FFT. A detailed description of the strategies used to obtain robust, accurate high frequency harmonic solutions in this paper can be found in Labaki et al. (2012).

Illustrative example

In order to illustrate the application of the FFT to obtain transient solutions for soil media, we considered initially the problem of a three-dimensional, isotropic, homogeneous half-space subjected to axisymmetric vertical unit loads of radius a, applied at the origin of the cylindrical (r,z) coordinate system. Influence functions of vertical displacement due to vertical loads for this medium have been derived by Rajapakse and Wang (1993) as:

$$u_{zz} = \delta^2 \int_0^\infty u^*_{zz}\zeta\, d\zeta, \tag{25}$$

in which

$$u^*_{zz} = -a_7 A \mathrm{e}^{-\delta\xi_1 z} - a_8 C \mathrm{e}^{-\delta\xi_2 z}, \tag{26}$$

in which $a_{7,8} = J_0(\delta\zeta r)\,\delta\xi_{1,2}$, in which J_i are Bessel functions of type 1 and order i, and

$$\xi_{1,2} = \frac{1}{\sqrt{2\alpha}}\left(\gamma\zeta^2 - 1 - \alpha \pm \sqrt{\Phi}\right)^{1/2}, \tag{27}$$

$$\Phi = \left(\gamma\zeta^2 - 1 - \alpha\right)^2 - 4\alpha\left(\beta\zeta^4 - \beta\zeta^2 - \zeta^2 + 1\right), \tag{28}$$

$$A = -C = \frac{b_{52}}{b_{21}b51 - b_{51}b_{22}}\frac{1}{\zeta} a J_1(\zeta a), \tag{29}$$

$$b_{21,22} = \left(\alpha\delta^2\xi_{1,2} - (\kappa - 1)\,\delta^2\zeta^2\theta_{1,2}\right) J_0(\delta\zeta r), \tag{30}$$

$$b_{51,52} = -\delta^2\xi_{1,2}\zeta(1 + \theta_{1,2}) J_1(\delta\zeta r), \tag{31}$$

and

$$\theta_{1,2} = \frac{\alpha\xi^2_{1,2}}{\kappa\zeta^2}. \tag{32}$$

For this illustration, we consider the isotropic case with $E = 2.5$ and $\nu = 0.25$, which results in $c_{11} = c_{33} = 3$ and $c_{12} = c13 = c_{44} = 1$, and $\rho = 1$. These properties correspond to a half-space in which shear and pressure waves travel

at velocities $c_s = (c_{44}/\rho)^{1/2} = 1$ and $c_p = (c_{12}/\rho)^{1/2} = 3$. Soil displacements u_{zz} are measured at a point of coordinates $(r = 5a, z = 0)$ at the surface of the soil. Two wave fronts are observed at this point, arriving from the nearest and from the farthest edge of the circular loading, which are located at a distance $d-a$ and $d+a$ from the measuring point, respectively.

Figure 3a shows the original response of the soil obtained in the frequency domain, and Fig. 3b shows the impulse response of the soil obtained by the method presented in this paper. The vertical lines in Fig. 3b mark the arrival of the pressure and shear wavefronts in dash-dotted and dashed lines, respectively. These are computed by determining the time that waves propagating at speeds c_p and c_s take to travel distances $d-a$ and $d+a$. Blue and red lines mark respectively the arrival of wavefronts from the nearest and farthest edges of the loading. These results are physically consistent with what is observed in engineering practice. At the time that the wavefronts are calculated to arrive, large disturbances are observed in the displacement of the measuring point. Larger disturbances are observed when shear waves arrive, which is also consistent. The bulk of the excitation of the measuring point occurs when the wavefronts from the farthest end of the loadings reach it, after which a monotonic decay of its displacement is observed.

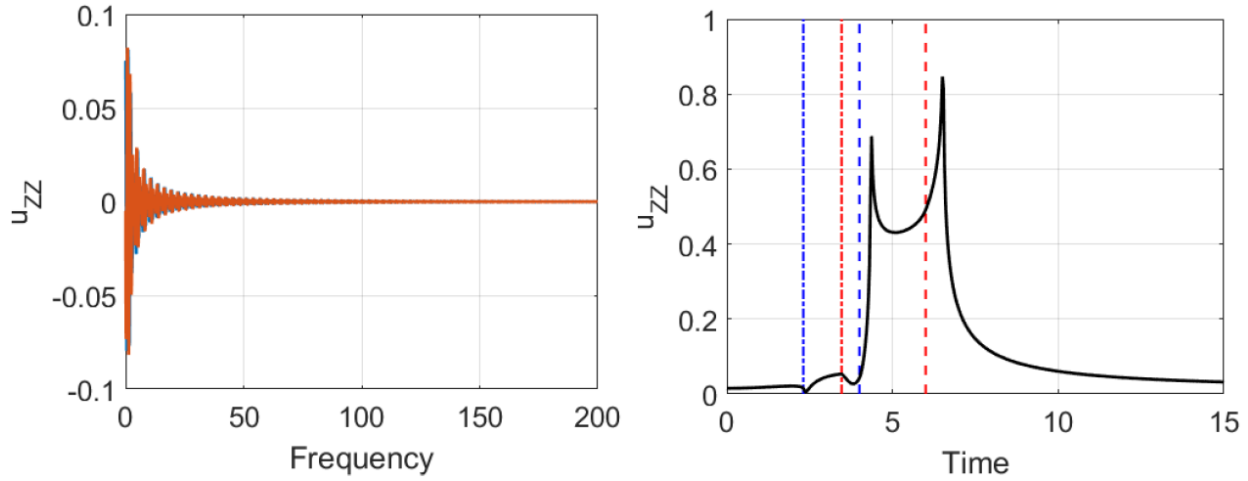

Figure 3 – Vertical displacement response of the 3D soil under vertical circular loads in the a) frequency domain and b) time domain.

Additionally, Fig. 4 shows the effect of including a small damping factor η into the soil. In this model, this is obtained via Christensen's elastic-viscoelastic correspondence principle (Christensen, 2010). The effect is the attenuation of the amplitude of its response, which is also physically consistent.

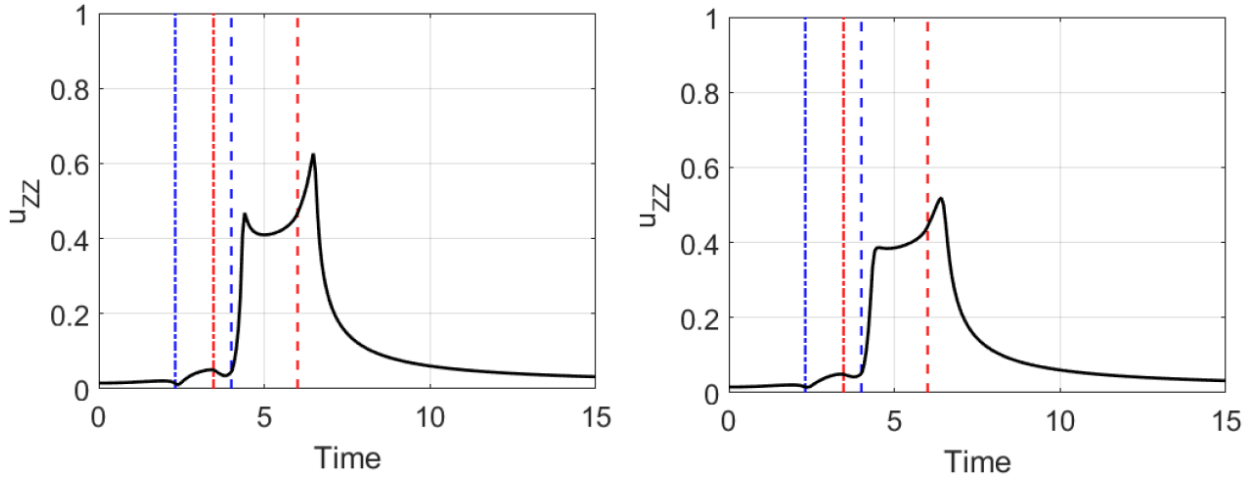

Figure 4 – Vertical displacement response of the 3D soil under vertical circular loads in the time domain for damping factor a) $\eta = 0.05$ **and b)** $\eta = 0.1$**.**

NUMERICAL RESULTS

This section considers the transient response of the half-plane before and after the inclusion of surface walls. These results consider a half-plane with material density $\rho = 1945\,\mathrm{kg/m^3}$, damping ratio $\eta = 0.025$, and material properties such that $c_s = 250\,\mathrm{m/s}$ and $c_p = 1470\,\mathrm{m/s}$. Two types of walls are consider. One is a gabion wall with $E_w = 367\,\mathrm{MPa}$, $\nu_w = 0.2$ and $\rho_w = 1700\,\mathrm{kg/m^3}$, and the other is a concrete wall with $E_w = 30{,}000\,\mathrm{MPa}$, $\nu_w = 0.2$ and $\rho_w = 2400\,\mathrm{kg/m^3}$. Walls of height $H = 2\,\mathrm{m}$ and $H = 3\,\mathrm{m}$ are considered. Results are measured at $x = 0$, referred to as "insertion point" (because it is where the wall is inserted), and at $x = 4\,\mathrm{m}$, referred to as "behind" the wall (because the wall is inserted between the loaded surface and this measuring point). In this analysis, loadings of width $a = 1\,\mathrm{m}$ are considered, which are applied at a distance $d = 4\,\mathrm{m}$ from the wall. These results are computed from a discrete signal of the harmonic response of the system from $\omega = 1$ to $\omega = 100\,\mathrm{Hz}$ containing $N = 100$ equally-spaced points.

Figures 5 and 6 show the response of the soil before and after the installation of the gabion wall. The responses include vertical and horizontal displacements due to vertical and horizontal loads. The results are all shown in the same scale to facilitate the comparison between the vibratory response of the system in different directions. Vertical dashed lines in these figures indicate the arrival of pressure (P) and shear (S) waves from the excitation source.

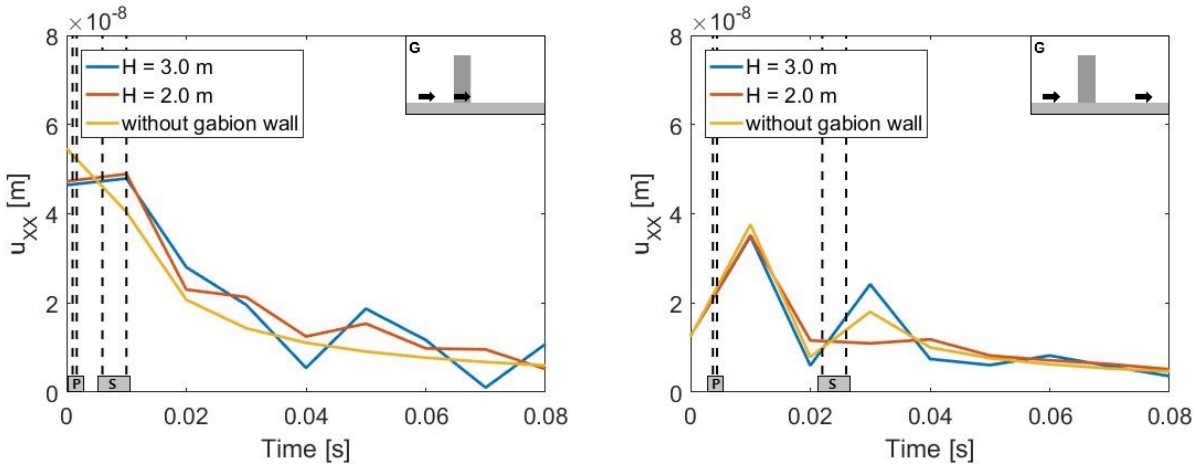

Figure 5 – Horizontal motion of the soil at a) $x = 0$ and b) $x = 4\,\mathrm{m}$ due to horizontal loads, before and after the installation of a gabion wall.

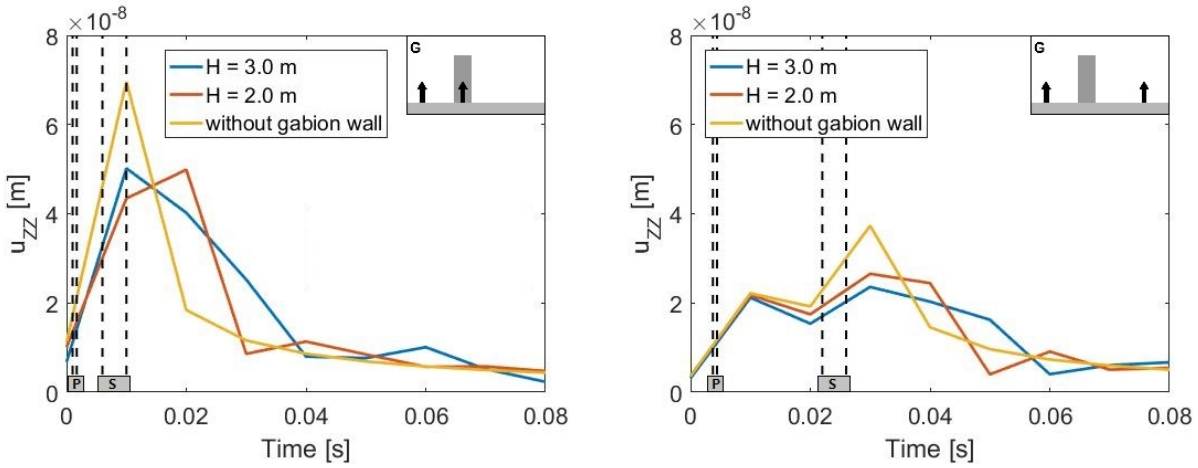

Figure 6 – Vertical motion of the soil at a) $x = 0$ and b) $x = 4\,\mathrm{m}$ due to vertical loads, before and after the installation of a gabion wall.

The results show that the response of the system is generally larger at the insertion point than at points behind the wall, which is expected due to the increased distance from the excitation source for $x = 4\,\mathrm{m}$. Vertical displacements due

to vertical loads (u_{ZZ}) have overall larger magnitudes than horizontal displacements due to horizontal loads (u_{XX}), as expected, in view of the increased flexibility of the soil in the vertical direction. Additionally, a spike in the magnitude of the responses is seen at the time when shear waves are expected to arrive. These are all physically consistent results.

As for the ground vibration attenuation performance of the wall, these results show that the walls do not provide a uniform reduction of the amplitude of motion of the wall throughout the observed period. For u_{ZZ}, a reduction of the amplitude of motion is observed around the arrival of the S wave, which is the instant in which the magnitude of ground motion is the largest. This reduction is also not a function of the height of the wall. The motion component that benefits the most from the inclusion of the wall is u_{ZZ}, the amplitude of which is reduced by 36% at the insertion point with the inclusion of a 2 m−tall gabion wall.

Figures 7 and 8 show the response of the soil before and after the installation of the concrete wall. The same overall attenuation performance that gabion walls had shown is observed also for concrete walls: concrete walls provide considerable attenuation at the time of the arrival of the S wave for the u_{ZZ} component, and provide otherwise negligible attenuation and sometimes an increase in the vibration amplitude of the system.

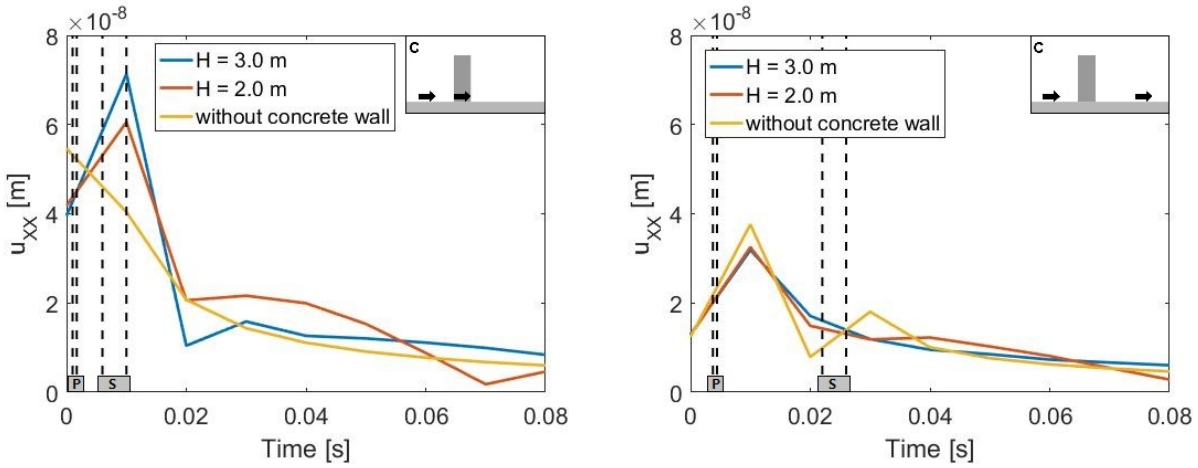

Figure 7 – Horizontal motion of the soil at a) $x = 0$ and b) $x = 4\,\mathrm{m}$ due to horizontal loads, before and after the installation of a concrete wall.

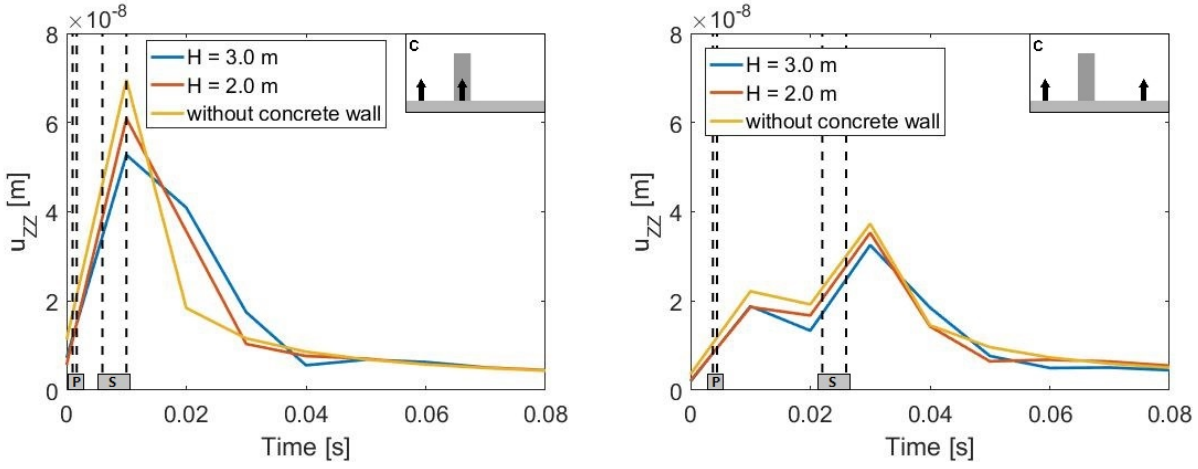

Figure 8 – Vertical motion of the soil at a) $x = 0$ and b) $x = 4\,\mathrm{m}$ due to vertical loads, before and after the installation of a concrete wall.

CONCLUSIONS

This paper presented a model of the transient response of surface walls interacting with the soil. The model consisted of an IBEM-FEM coupled approach to obtain the response of the wall–soil system in the frequency domain, together with a FFT to extract the response of the model to impulse loads. The model was used to analyze the problem of ground vibration attenuation performance of the wall. Gabion and concrete walls of different heights were considered. The results showed that surface walls are capable of providing significant attenuation of ground vibration at both the insertion point and at points behind the wall at the instant in which its magnitude is the largest. However, no correlation was found between the constitutive and geometric properties of the wall and their overall attenuation performances for the parameters considered in the present analysis.

REFERENCES

Álamo, G. M., Bordón, J. D., Aznarez, J. J., Lombaert, G., 2019. "The effectiveness of a pile barrier for vibration transmission in a soil stratum over a rigid bedrock. Computers and Geotechnics 110, 274–286.

Albino, C., Godinho, L., Amadomendes, P., AlvesCosta, P., Dias da Costa, D., Soares Jr., D., 2019. "3D FEM analysis of the effect of buried phononic crystal barriers on vibration mitigation. Engineering Structures 196.

Bathe, K.J., 2006. "Finite element procedures." Prentice Hall.

Bose, T., Choudhury, D., Sprengel, J., Ziegler, M., 2018. "Efficiency of open and infill trenches in mitigating ground-borne vibrations." Journal of Geotechnical and Geoenvironmental Engineering 144.

Carneiro, D., Barros, P. L. A., Labaki, J., 2022. "Ground vibration attenuation performance of surface walls". Computers and Geotechnics, 1:28.

Carneiro, D., Labaki, J., Hoefel, S. S., Barros, P. L. A. "Dynamic Displacement and Strain Fields within Trenched Soils: Post-Processing Quantities from Indirect-BEM's Fictitious Loads." In: Iberian Latin American Congress on Computational Methods in Engineering, CILAMCE 2019.

Casablanca, O., Ventura, G., Garesci, F., Azzerboni, B., Chiaia, B., Chippini, M., Finocchio, G., 2018. "Seismic isolation of buildings using composite foundations based on metamaterials." Journal of Applied Physics 123.

Christensen, R. M., 2010. "Theory of Viscoelasticity: Second Edition" (Dover Civil and Mechanical Engineering). Dover Publications.

Colombi, A., Roux, P., Guenneau, S., Gueguen, P., Craster, R.V., 2016. "Forests as a natural seismic metamaterial: Rayleigh wave bandgaps induced by local resonances." Scientific reports 6.

Dijckmans, A., Coulier, P., Jiang, J., Toward, M., Thompson, D., Degrande, G., Lombaert, G., 2015. "Mitigation of railway induced ground vibration by heavy masses next to the track." Soil Dynamics and Earthquake Engineering 75, 158–170.

Herbut, A., 2020. "Vibration mitigation efficiency of an inclined, curved, open trench." Plos one 15.

Kaewunruen, S., Aikawa, A., Remennikov, A. M., 2017. "Vibration attenuation at rail joints through under sleeper pads." Procedia engineering 189, 193–198.

Krylov, V. V., 2007. "Control of traffic-induced ground vibrations by placing heavy masses on the ground surface." Journal of low frequency noise, vibration and active control 26, 311–321.

Labaki, J., Romanini, E., and Mesquita, E., 2012. "Stationary dynamic displacement solutions for a rectangular load applied within a 3D viscoelastic isotropic full space - Part II: Implementation, validation, and numerical results". Mathematical Problems in Engineering.

Masoumi, H., Van Leuven, A., Urbaniak, S., 2014. "Mitigation of train induced vibrations by wave impeding blocks: numerical prediction and experimental validation." EURO5DYN 2014 , 863–870.

Mhanna, M., Shahrour, I., Sadek, M., Dunez, P., 2014. "Efficiency of heavy mass technology in traffic vibration reduction: Experimental and numerical investigation." Computers and Geotechnics 55, 141–149.

Rajapakse, R., Wang, Y., 1991. "Elastodynamic Green's functions of orthotropic half plane." Journal of engineering mechanics 117, 588–604.

Rajapakse, R. K. N. D., Wang, Y., 1993. "Green's functions for transversely isotropic elastic half space." Journal of Engineering Mechanics, 119(9), 1724-1746.

RESPONSIBILITY NOTICE

The authors are the only parties responsible for the printed material included in this paper.